Interface reconfiguration of $MnCO_3/Mn_3O_4$ heterostructure enhances the ozone decomposition in the entire humidity range

Yani Zhang [a], Ning Cao [a], Hao Cheng [c], Xinben Zhao [c], Lixia Qiu [c], Yunlong Fang [d], Jiahong Liao [a], Xinuo Cai [a], Xiangyu Tian [a], Lecheng Lei [a,b], Pengfei Xie [a,b,*], Xingwang Zhang [a,b,*]

[a] Key Laboratory of Biomass Chemical Engineering of Ministry of Education, College of Chemical and Biological Engineering, Zhejiang University, Hangzhou 310027, China
[b] Institute of Zhejiang University-Quzhou, Quzhou 324000, China
[c] Zhejiang Quzhou Jusu Chemical Co., Ltd., Quzhou 324004, China
[d] Zhejiang Qingke Environmental Protection Technology Co., Ltd., Quzhou 324004, China

ARTICLE INFO

ABSTRACT

The catalytic efficiency of manganese-based catalysts in practical ozone decomposition applications is limited by challenging desorption of intermediate oxygen species and competitive adsorption of H_2O molecules in humid environments. In this work, $MnCO_3/Mn_3O_4$ composites with heterogeneous structures were synthesized through a facile one-step strategy. The obtained $MnCO_3/Mn_3O_4$-1/2 catalyst exhibited high content of oxygen vacancies, fast electron mobility rate and obvious advantages in catalytic ozone decomposition performance at a space velocity of 600 L g^{-1} h^{-1} and 95% RH. In-situ DRIFT spectra indicated that the rate-determining steps for ozone decomposition of $MnCO_3$ and Mn_3O_4 are the reaction of atomic oxygen with ozone to form O_2^{2-} and desorption of O_2^{2-}, respectively. $MnCO_3/Mn_3O_4$ heterogeneous catalyst undergoes reconfiguration under ozone atmosphere, inducing discontinuous MnO_x coatings on the $MnCO_3$ surface, which form a potential difference with Mn_3O_4. $MnCO_3/Mn_3O_4$ heterogeneous structure modulates the electronic state of active site, and the synergistic effect of $MnCO_3$ and Mn_3O_4 improves catalytic performance.

1. Introduction

Ozone is a typical air pollutant that is regulated by the World Health Organization (WHO) and is subjected to regulations in numerous countries [1]. People are exposed to ozone almost all the time, and it is formed outdoors by the photochemical reaction between nitrogen oxides (NO_x) and volatile organic compounds (VOCs), as well as produced by a variety of household electrical appliances, including photocopiers, laser printers, sterilizers and air purifiers [2,3]. In recent years, the widespread contamination of ground-level ozone has gained global attention due to its detrimental effects on human health [4–6]. Owing to its potent oxidation and high reactivity, exposure to both long and short-term ozone has been associated with increased morbidity, including respiratory, cardiovascular, as well as cardiopulmonary diseases. In addition to the direct hazards, a series of ozone reactions can lead to the formation of secondary pollutants, including organic aerosols, aldehydes, and carboxylic acids, which can pose a greater risk to

human health than ozone itself [7,8]. Consequently, there is an urgent need to develop efficient and environmentally friendly methods applicable to the elimination of ozone pollution at ground level for both public health and ecosystems.

Generally, ozone elimination method refers to the process of breaking down ozone molecules into oxygen molecules using an appropriate reaction condition, which can be accomplished through several techniques, including photolysis, thermal destruction, liquid adsorption, or catalytic decomposition [9–11]. Catalytic decomposition is widely explored due to its high efficiency, mild reaction conditions, environmentally friendly and no energy consumption [12–14]. In particular, Manganese-based materials are widely researched as catalysts for ozone owing to their relatively low cost and high efficiency, compared with noble metal and other transition metal oxide catalysts [15,16]. Dhandapani and Oyama [12] summarized a range of metal oxides reported in the literature, indicating that manganese oxide (MnO_x) as the active component exhibited significantly better properties

for ozone decomposition than other transition metal oxides. Subsequently, several types of research demonstrated that the catalytic performance of MnO_x in ozone decomposition depends upon its diverse valence states, multiple structures, and surface oxygen vacancies [17, 18]. Due to the wide valence distribution of manganese in MnO_x, redox couples, and oxygen vacancies, which play a critical role in the ozone decomposition reaction, are readily generated [19–21]. Additionally, it remains a challenge for catalysts to remove ozone in the presence of H_2O molecules competing for adsorption since the ozone decomposition efficiency of the catalysts in humid environments is greatly reduced. For instance, the ozone decomposition efficiency of MnO_2 decreased from 100 % to 90 % and 60 % as the relative humidity (RH) increased from 10 % to 50 % and 90 % [22]. Therefore, it is imperative to develop catalytic materials with high stability at room temperature that are resistant to the effects of H_2O molecules.

Compared to MnO_x, $MnCO_3$ has attracted widespread attention as a desulfurization catalyst and anode material in the battery field, owning to its abundant raw materials, high thermal stability, and high practical capability [23–25]. In addition, $MnCO_3$ commonly serves as a precursor for the preparation of MnO_x via heat treatment or alternative techniques. Luciano et al. [26] synthesized MnO_x for the oxidative decomposition of ethanol utilizing $MnSO_4$ and $MnCO_3$ as precursors, and the results indicated that the γ-MnO_2 catalyst fabricated with $MnCO_3$ presented higher catalytic performance and a simpler preparation process. For the ozone decomposition reaction, Jia et al. [27] synthesized submicron $MnCO_3$ spheres via co-precipitation and discovered that with the degradation of ozone, a layer of MnO_x was swiftly formed on the surface as the primary active substance for decomposing ozone. Furthermore, Liu et al. [28] obtained $MnCO_3$/MnO_2 using $MnCO_3$ as precursor by simple heat treatment, which exhibited better ozone degradation performance than commercial α-MnO_2 catalysts in the presence of water due to its richer oxygen vacancies and strong Lewis-acid sites. Accordingly, it inspired us to construct $MnCO_3$-MnO_x composites to regulate the adsorption state of intermediate oxygen species and H_2O molecules on the catalyst surface during the reaction process by modifying the electronic state of the catalyst's active sites, thus improving the ozone decomposition performance.

Herein, a high-performance catalyst ($MnCO_3$/Mn_3O_4) with a heterogeneous structure was developed through a facile and green co-precipitation method and applied to remove ozone at a full range of humidity. The heterogeneous interfacial electronic structure was optimized by adjusting the ratio of OH^-/CO_3^{2-} in the precursor solution, and the obtained $MnCO_3$/Mn_3O_4-1/2 catalyst exhibited a high content of oxygen vacancies and fast electron mobility rate. The $MnCO_3$/Mn_3O_4-1/2 catalyst showed excellent and stable catalytic efficiency at 20 ppm inlet ozone concentration, 600 L g^{-1} h^{-1} space velocity, and room temperature, achieving 100 % ozone decomposition conversion after 100 h of reaction at 40 % RH and sustaining more than 95 % conversion after 100 h of reaction at 95 % RH. During the ozone decomposition reaction, the interfacial effect of the $MnCO_3$/Mn_3O_4 heterogeneous structure modulates the electronic state of the active site and enhances the rate of electron migration. The in-situ DRIFT outcomes demonstrate that the rate-controlling mechanisms of the ozone decomposition reactions of $MnCO_3$ and Mn_3O_4 are the reaction between atomic oxygen and ozone to form intermediate oxygen species (O_2^{2-}) and the subsequent desorption of O_2^{2-}, respectively. Moreover, the $MnCO_3$/Mn_3O_4 heterogeneous catalyst undergoes reconfiguration under the ozone atmosphere, inducing discontinuous MnO_x coatings on the $MnCO_3$ surface, which form a potential difference with Mn_3O_4. The synergistic effect of $MnCO_3$ and Mn_3O_4 accelerates these two rate-determining steps, thereby increasing the reaction efficiency. This provides a deeper understanding of the ozone decomposition process and contributes to the practical application of manganese-based catalysts.

2. Experimental section

2.1. Synthesis of $MnCO_3$/Mn_3O_4

$MnCO_3$/Mn_3O_4 composite catalysts were synthesized by a facile co-precipitation method. $Mn(NO_3)_2$ (0.02 mol) was first mixed with H_2O (70 mL) to form a homogeneous solution A. At the same time, 70 mL of a mixed solution containing NaOH and Na_2CO_3 (CO_3^{2-}/OH^- molar ratio = 2/1, 1/2) was taken and named solution B. Then, solution A and solution B were dropped into 50 mL of deionized water drop by drop at the same time, and the pH of the resulting slurry was maintained at approximately 9. The mixture was then allowed to crystallize in a water bath at 90 °C for 24 h. The final precipitate was filtered, washed thoroughly with deionized water and freeze-dried for 24 h. The catalysts were named $MnCO_3$/Mn_3O_4-2/1 and $MnCO_3$/Mn_3O_4-1/2.

2.2. Synthesis of $MnCO_3$ and Mn_3O_4

$MnCO_3$ and Mn_3O_4 catalysts were synthesized using the same method as the $MnCO_3$/Mn_3O_4 composites catalysts, except for solution B with 0.02 mol of Na_2CO_3 or 0.05 mol NaOH in 70 mL of deionized water to be dropped into 50 mL of deionized water drop by drop with solution A.

2.3. Characterization methods

SEM, TEM, XRD and BET were used to analyze the microstructure and chemical properties of materials. XPS, EPR, CV, EIS and UV–vis were used to investigate surface atomic states, oxygen vacancies, and electron mobility. Electrochemical measurements were carried out with O_2-saturated 0.5 M H_2SO_4 as the electrolyte with a standard three-electrode system. In-situ DRIFTS were used to confirm the dynamic decomposition process of O_3 under dry and humid conditions. (For detailed preprocessing and test conditions, please refer to the Supporting Information).

2.4. Catalytic performance evaluation

For detailed procedures and parameters, see the Supporting Information. Unless otherwise stated, the reaction conditions were as follows: a feed gas of 0.3 L·min^{-1} with 5 % - 95 % of RH, containing 20 ppm of ozone, flowed through the catalyst bed, which corresponds to a space velocity of 600 L g^{-1} h^{-1}. Ozone conversion was calculated by the following equation:

Ozone conversion (%) = (C_{in} - C_{out}) / C_{in} × 100 %;

where C_{in} and C_{out} were the inlet and outlet concentrations of ozone, respectively.

3. Results and discussion

3.1. Structure characterization of catalysts

The $MnCO_3$, Mn_3O_4 and $MnCO_3$/Mn_3O_4 composite catalysts were provided by adjusting the molar ratio of CO_3^{2-}/OH^- through the co-precipitation method, and the detailed fabrication is schematically illustrated in Fig. 1a. Notably, the pH of all precursor solutions was maintained at 9.0 using 0.1 M NaOH or 0.1 M HNO_3 before crystalline aging. The XRD pattern (Fig. 1b) displays the formation of single crystals of $MnCO_3$ and Mn_3O_4 with the addition of only Na_2CO_3 and NaOH, respectively. As shown in Fig. 1c, a series of diffraction peaks with the positions at 24.3°, 31.4° and 51.7° of the as-obtained composite catalysts, which could be assigned to (012), (104) and (116) lattice planes from rhodochrosite $MnCO_3$ phase (PDF card no. 44–1472) [29]. Additionally, the other diffraction peaks appear at 18°, 28.8°, 32.3° and
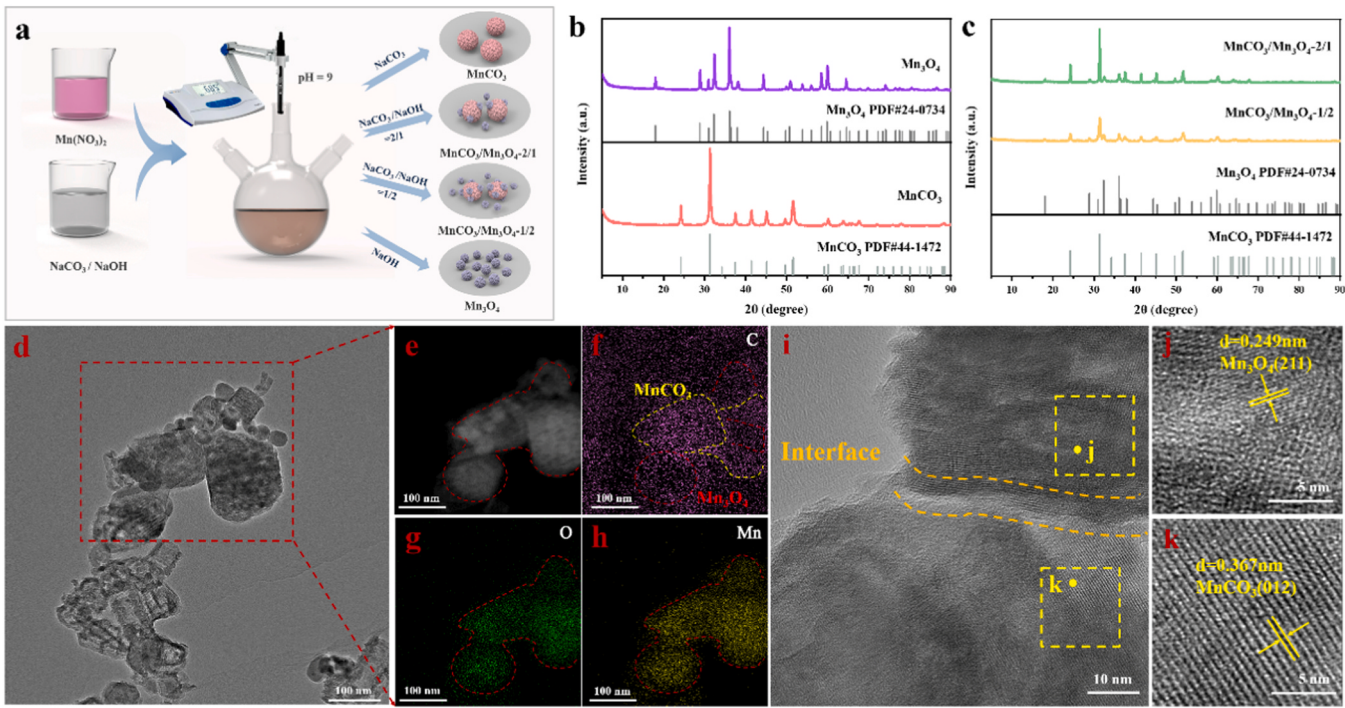
Fig. 1. (a) Schematic illustration of the preparation process of $MnCO_3$, $MnCO_3/Mn_3O_4$-2/1, $MnCO_3/Mn_3O_4$-1/2 and Mn_3O_4 catalysts. (b, c) XRD patterns for $MnCO_3$, $MnCO_3/Mn_3O_4$-2/1, $MnCO_3/Mn_3O_4$-1/2 and Mn_3O_4 catalysts. (d) TEM image, (e-h) HAADF-STEM image and corresponding elemental mapping images, and (i-k) HRTEM images of $MnCO_3/Mn_3O_4$-1/2.

$36.1°$, which are attributed to (101), (112), (103) and (211) reflections of Mn_3O_4 (PDF card no. 24–0734), demonstrating that the composite catalysts with two crystal forms of $MnCO_3$ and Mn_3O_4 were successfully synthesized [30].

The morphologies of $MnCO_3$, Mn_3O_4, and $MnCO_3/Mn_3O_4$ composite catalysts were studied in Fig. S1. The overall morphology of $MnCO_3$ and Mn_3O_4 exhibits a spherical structure composed of stacked nanosheets and a dispersed nanosheet structure, respectively. Compared to $MnCO_3$, the flowery spherical structure of $MnCO_3/Mn_3O_4$-2/1 became irregular. With the increase of NaOH content in the precursor salt solution, the morphology of $MnCO_3/Mn_3O_4$-1/2 exhibits columnar structures of about 3–4 μm in length with additional nanoparticles precipitated on and around the surface. In addition, the N_2 adsorption-desorption isotherms are shown in Fig. S2 and Table S1, the $MnCO_3/Mn_3O_4$-2/1 (S_{BET} = 51.25 m^2g^{-1}) and $MnCO_3/Mn_3O_4$-1/2 (S_{BET} = 59.39 m^2g^{-1}) composite catalysts have a higher specific surface area compared with $MnCO_3$ and Mn_3O_4 [29,31]. Therefore, it is speculated that the OH^-/CO_3^{2-} ratio in the precursor salt solution during preparation affects the crystal nucleation and growth direction.

To reveal the structure of the composite catalyst more intuitively, HAADF-STEM and HRTEM characterization was carried out. Specifically, Fig. 1d-h display the STEM images of $MnCO_3/Mn_3O_4$-1/2 composite catalyst, and the elemental mapping result of C confirms that $MnCO_3/Mn_3O_4$-1/2 consists of $MnCO_3$ and Mn_3O_4 nanoparticles aggregates and forms a heterogeneous structure. The HRTEM image shown in Fig. 1i corresponds to the position of the interface between the two phases in the STEM image, showing two sets of distinct lattice fringes corresponding to $MnCO_3$ (012) plane and Mn_3O_4 (211) plane, respectively [30]. Furthermore, the HRTEM images of $MnCO_3/Mn_3O_4$-2/1 also illustrate two sets of distinct lattice fringes corresponding to $MnCO_3$ (012) plane and Mn_3O_4 (211) plane, as shown in Fig. S3. The results above verify that the $MnCO_3/Mn_3O_4$-2/1 and $MnCO_3/Mn_3O_4$-1/2 composite catalysts have successfully constructed $MnCO_3/Mn_3O_4$ heterogeneous structure.

To investigate the differences in the electronic structure of the series

of catalysts, X-ray photoelectron spectrum (XPS) was performed. The Mn 2p and Mn 3 s spectra of these four catalysts deconvoluted with the Gaussian peak fitting method are recorded and displayed in Fig. 2a-b. The Mn $2p_{3/2}$ peak of $MnCO_3$ is deconvoluted into two sub-peaks with the binding energy at 640.7 and 644.2 eV, which are attributed to Mn^{2+} and a satellite peak, respectively (Fig. 2a) [32]. Notably, The Mn $2p_{3/2}$ peak of $MnCO_3/Mn_3O_4$-2/1, $MnCO_3/Mn_3O_4$-1/2 and Mn_3O_4 catalysts are deconvoluted into three sub-peaks with the binding energy at 640.5, 641.8 and 644.0 eV, which are attributed to Mn^{2+}, Mn^{3+} and a satellite peak, respectively [21,33]. As illustrated in Table 1, the Mn^{2+}/Mn^{3+} ratio of $MnCO_3/Mn_3O_4$-2/1 (1.01) and $MnCO_3/Mn_3O_4$-1/2 (1.09) were similar. Furthermore, Mn 3 s signals were also employed to distinguish the oxidation states of Mn (Fig. 2b). In terms of the formula AOS = $8.956 - 1.126$ ΔE, Mn atoms of $MnCO_3/Mn_3O_4$-1/2 (2.18) possess a lower oxidation state compared to $MnCO_3/Mn_3O_4$-2/1 (2.21), and both are intermediate between $MnCO_3$ (1.96) and Mn_3O_4 (2.59) [10]. This result is consistent with the Mn 2p spectrum, where the valence state of Mn in the $MnCO_3/Mn_3O_4$ composite catalyst is between that of single-phase $MnCO_3$ and Mn_3O_4. Significantly, as the XPS results are based on surface analysis, for the composite catalysts, when the ratio of OH^-/CO_3^{2-} is increased, the catalysts with lower $MnCO_3$ content have a higher Mn^{2+}/Mn^{3+} ratio and a lower AOS of Mn. This suggests that a heterogeneous interfacial structure is formed between $MnCO_3$ and Mn_3O_4, and there is electron transfer at the interface.

In addition, the O1s spectra of catalysts were also given to provide a preliminary understanding of the catalyst oxygen vacancy content. As shown in Fig. 2c, the O 1 s spectrum of $MnCO_3$ located at 530.4 eV is assigned to CO_3^{2-} and that of Mn_3O_4 deconvoluted into two peaks at ~529.5 and ~531.1 eV could be attributed to oxide lattice oxygen (O_α) and surface-absorbed oxygen species (O_β), respectively [34–36]. Notably, as for $MnCO_3/Mn_3O_4$ composite catalysts, three peaks with different intensities are located at 529.4, 530.5 and 531.2 eV, corresponding to the O_α, CO_3^{2-} and O_β, respectively, and the O_β/O_α ratio was displayed in Table 1. It is noteworthy that $MnCO_3/Mn_3O_4$-1/2 (0.51) showed a much higher O_β/O_α ratio, compared to $MnCO_3/Mn_3O_4$-2/1
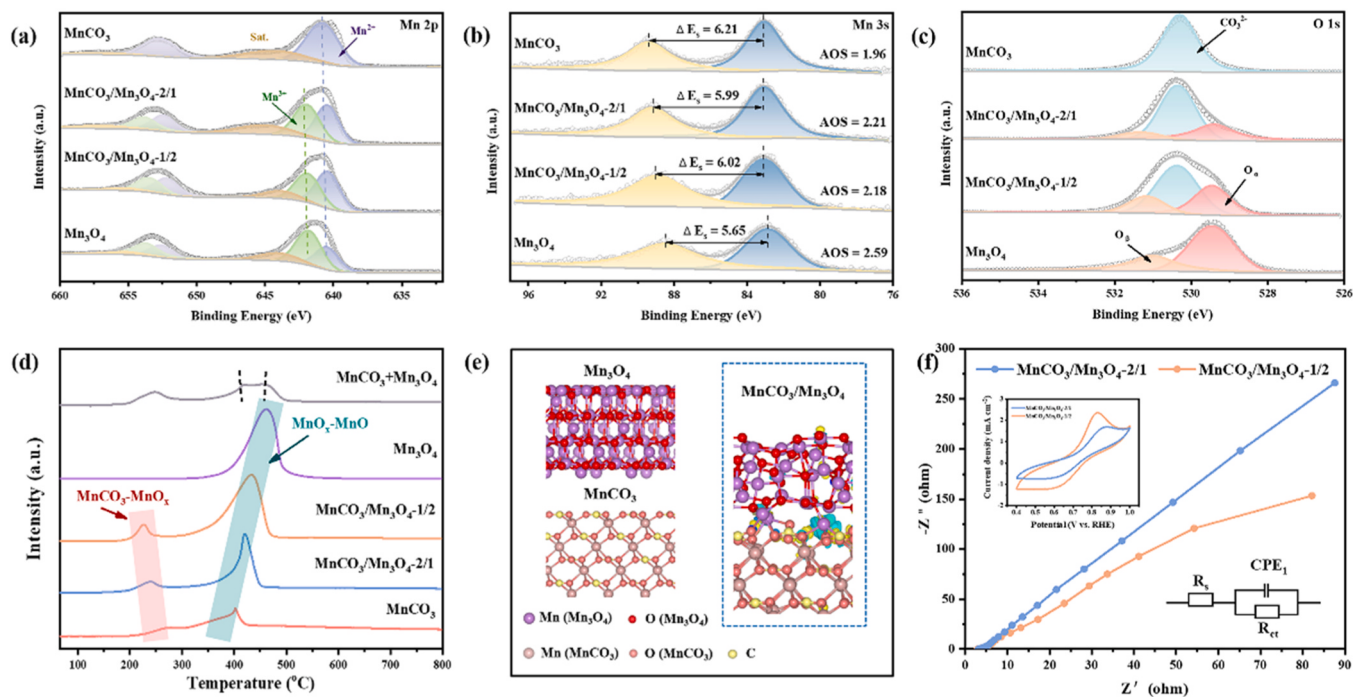
Fig. 2. (a-c) XPS spectra of Mn 2p, Mn 3 s and O 1 s for $MnCO_3$, $MnCO_3/Mn_3O_4$-2/1, $MnCO_3/Mn_3O_4$-1/2 and Mn_3O_4 catalysts. The fwhm of the same metal element remains constant. (d) H_2-TPR profiles of $MnCO_3$, $MnCO_3/Mn_3O_4$-2/1, $MnCO_3/Mn_3O_4$-1/2, Mn_3O_4 and $MnCO_3+Mn_3O_4$ catalysts. (e) Differential charge density of $MnCO_3/Mn_3O_4$ calculated by Density Functional Theory (DFT) (the cyan color shows the charge depletion and the yellow color shows the charge accumulation) and (f) Nyquist plots for $MnCO_3/Mn_3O_4$-2/1 and $MnCO_3/Mn_3O_4$-1/2 catalysts (inset: CV curves and equivalent circuit).

Table 1

Mn 2p and 3 s electrons binding energies, proportion of Mn species with different valences and O_β/O_α ratio in series catalysts by XPS measurements.

Catalysts	Mn-$2p_{3/2}$			Mn-3 s	O-1 s
	Mn^{2+} (%)	Mn^{3+} (%)	$Mn^{2+}/$ Mn^{3+}	AOS of Mn	$O_\beta/$ O_α
$MnCO_3$	100	——	——	1.96	——
$MnCO_3/Mn_3O_4$- 2/1	50.16	49.84	1.01	2.21	0.38
$MnCO_3/Mn_3O_4$- 1/2	52.23	47.77	1.09	2.18	0.51
Mn_3O_4	39.07	60.93	0.64	2.59	0.45

(0.38) and Mn_3O_4 (0.45), which represents more oxygen vacancies. Compared with $MnCO_3/Mn_3O_4$-2/1, although $MnCO_3/Mn_3O_4$-1/2 has a higher Mn_3O_4 content, it has a higher Mn^{2+}/Mn^{3+} ratio and a lower Mn AOS due to the regulation of the interfacial structure, which makes the surface of $MnCO_3/Mn_3O_4$ form more abundant oxygen vacancies to maintain electrostatic equilibrium.

To further verify the electron transfer at the interface of the heterostructure, H_2-TPR tests were carried out on the series of catalysts. As shown in Fig. 2d, $MnCO_3$ showed two major hydrogen depletion peaks at about 260 °C and 405 °C, which were attributed to the pyrolysis of $MnCO_3$ and the reduction of MnO_x-MnO, where MnO_x is a pyrolysis product of $MnCO_3$. Mn_3O_4 showed hydrogen depletion peaks only at about 460 °C, which was attributed to the reduction of Mn_3O_4-MnO. In addition, the mixed catalyst ($MnCO_3 + Mn_3O_4$) obtained by physically mixing $MnCO_3$ with Mn_3O_4 showed three major hydrogen depletion peaks at 260 °C, 405 °C and 460 °C. Notably, both $MnCO_3/Mn_3O_4$-2/1 and $MnCO_3/Mn_3O_4$-1/2 composite catalysts showed only two hydrogen consumption peaks at 230 °C and 430 °C, which is strong evidence that significant interactions occur at the $MnCO_3/Mn_3O_4$ interface due to the presence of heterostructures, which promotes electron transfer. In addition, the electron transfer at the interface of the heterostructure was

simulated using density functional theory (DFT). The differential charge density of the $MnCO_3/Mn_3O_4$ heterostructure shows a significant concentration of electrons near $MnCO_3$ (Fig. 2e), revealing that the electron-rich sites are mainly located at the interface of the heterostructure and electrons migrate from Mn_3O_4 to $MnCO_3$ at the interface due to interfacial effects of the heterostructure. The results of H_2-TPR and DFT indicate that the formation of heterogeneous structures in the $MnCO_3/$ Mn_3O_4 composite catalysts leads to significant electron transfer at the interface, which alters the electronic structure of the Mn sites.

According to the information on $MnCO_3/Mn_3O_4$ heterogeneous structure over composite catalysts, cyclic voltammetry (CV) was conducted to contrast the concentration of oxygen vacancies and electron mobility in the two composite catalysts. As shown in Fig. 2f, the higher oxidation peak area of $MnCO_3/Mn_3O_4$-1/2 compared with that of $MnCO_3/Mn_3O_4$-2/1 indicates a higher content of surface oxygen vacancies [37,38]. The current of $MnCO_3/Mn_3O_4$-1/2 was much higher than that of $MnCO_3/Mn_3O_4$-2/1, which proved that $MnCO_3/Mn_3O_4$-1/2 had a stronger electron transfer ability. In addition, electrochemical impedance spectroscopy (EIS) was used to investigate the electron transfer kinetics on the surface of the heterogeneous interfacial structure [39]. According to the EIS, the Nyquist circle radii follow this order: $MnCO_3/Mn_3O_4$-2/1 > $MnCO_3/Mn_3O_4$-1/2, which indicates that the electron transfer resistance is smaller and the electron mobility rate is faster in $MnCO_3/Mn_3O_4$-1/2. The optimized resistance is associated with the electronic interaction between the $MnCO_3$ and Mn_3O_4 interfaces within the composite catalysts, which influences electron transfer. Furthermore, the UV–vis spectra and the Tauc equation (Fig. S4) show that the band gaps of $MnCO_3/Mn_3O_4$-2/1 and $MnCO_3/Mn_3O_4$-1/2 are 3.74 eV and 3.27 eV, correspondingly, signifying that $MnCO_3/Mn_3O_4$-1/2 is more susceptible to electron migration [40,41]. The above results indicate that the optimization of the heterogeneous interfacial structure of the composite catalysts by adjusting the OH^-/CO_3^{2-} ratio can increase the concentration of surface oxygen vacancies and significantly affect the rate of electron transfer between $MnCO_3$ and Mn_3O_4.

Based on the above characterization results, it was deduced that the catalyst structure could be optimized by changing the proportion of the precursor salt solution. When precipitated with only Na_2CO_3, due to the hydrolysis of CO_3^{2-}, a certain amount of OH^- ions are present in the solution and Mn^{2+} reacts with CO_3^{2-} under alkaline conditions leading to the formation of $MnCO_3$. However, when NaOH is used alone as a precipitant, Mn^{2+} initially forms $Mn(OH)_2$ and $MnOOH$, which subsequently transforms into Mn_3O_4 throughout the aging process [30]. It is worth noting that $Mn(NO_3)_2$ is a strong acid and weak base salt, which causes the hydrolyzed solution of Mn^{2+} to turn acidic, and there is a process of re-nucleation and re-growth in the preparation of the catalysts. In addition, the richer interfaces formed during the re-nucleation and re-growth process of heterostructure catalysts greatly facilitate the electron transfer between $MnCO_3$ and Mn_3O_4. By adjusting the OH^-/CO_3^{2-} ratio in the precursor salt solution, the electronic structure of $MnCO_3/Mn_3O_4$ composite catalysts can be optimized, which leads to an increase in the oxygen vacancy concentration and electron mobility.

## 3.2. Catalytic performance in ozone decomposition

Water molecules were selected as impurity molecules and ozone conversion was evaluated for various samples at ambient temperature (25 °C) and full range of humidity. As demonstrated in Fig. 3, the ozone conversion rate of all catalysts decreases with reaction time, under both dry and wet reaction conditions. This can be attributed to the accumulation of oxygen intermediates and the adsorption of H_2O on active sites, which ultimately leads to catalyst deactivation. The graph in Fig. 3a displays the efficiency of $MnCO_3$, Mn_3O_4 and $MnCO_3/Mn_3O_4$ composite catalysts in decomposing ozone at 5 % RH (Relative Humidity). Except for $MnCO_3$, all the catalysts illustrated superior and sustained efficiency for 5 h. At a humidity of 95 %, $MnCO_3/Mn_3O_4$-1/2 sustained a 100 % ozone depletion rate for 5 h, as illustrated in Fig. 3b. However, the ozone conversion rates of $MnCO_3$, Mn_3O_4 and $MnCO_3/Mn_3O_4$-2/1 decreased to

28.2 %, 63.1 % and 82.8 % after 5 h, respectively, indicating that their catalytic performance in the process of decomposing ozone is insufficient. It is noteworthy that the degradation performance of $MnCO_3$ towards ozone under different humidity conditions was slightly decreased, while the performance of Mn_3O_4 was drastically decreased, as shown in Fig. 3c. It is speculated that the possible reason for this phenomenon is the low activity of $MnCO_3$, which leads to insignificant changes in its performance. Furthermore, the composite catalysts, especially $MnCO_3/Mn_3O_4$-1/2, displayed excellent performances during ozone decomposition under different humidity compared to $MnCO_3$ and Mn_3O_4.

To further investigate the influence of heterogeneous structure on the catalytic efficacy of $MnCO_3/Mn_3O_4$ composite catalysts, $MnCO_3+Mn_3O_4$ catalysts mixed in similar ratios were tested for their performance under 95 % RH conditions. As shown in Fig. S5, the catalytic performance of $MnCO_3+Mn_3O_4$ catalysts in ozone decomposition was intermediate compared to $MnCO_3$ and Mn_3O_4 and significantly lower compared to $MnCO_3/Mn_3O_4$ composite catalysts. Therefore, the excellent performance of the $MnCO_3/Mn_3O_4$ composite catalysts should be attributed to the heterogeneous interfacial structures. These results suggest that heterogeneous structures with interfacial electron transfer rather than simple two-phase mixing can significantly improve the ozone decomposition efficiency.

The ozone stability of better-performing $MnCO_3/Mn_3O_4$-1/2 composite catalyst was also investigated. The stability of the catalyst was tested for ozone degradation at different concentrations, at 95 % relative humidity and a space velocity of 600 L g^{-1} h^{-1} (Fig. 3d). The results showed that at 20 ppm ozone concentration, the $MnCO_3/Mn_3O_4$-1/2 catalyst successfully maintained complete ozone conversion in the first 70 hours, and safely maintained over 95 % conversion even after 100 hours without significant deactivation. In contrast, for 150 ppm ozone, the ozone conversion of $MnCO_3/Mn_3O_4$-1/2 rapidly decreased to less than 60 % within 18 h and remained at 40 % after 100 h, illustrating that it has stable high and stable performance in the
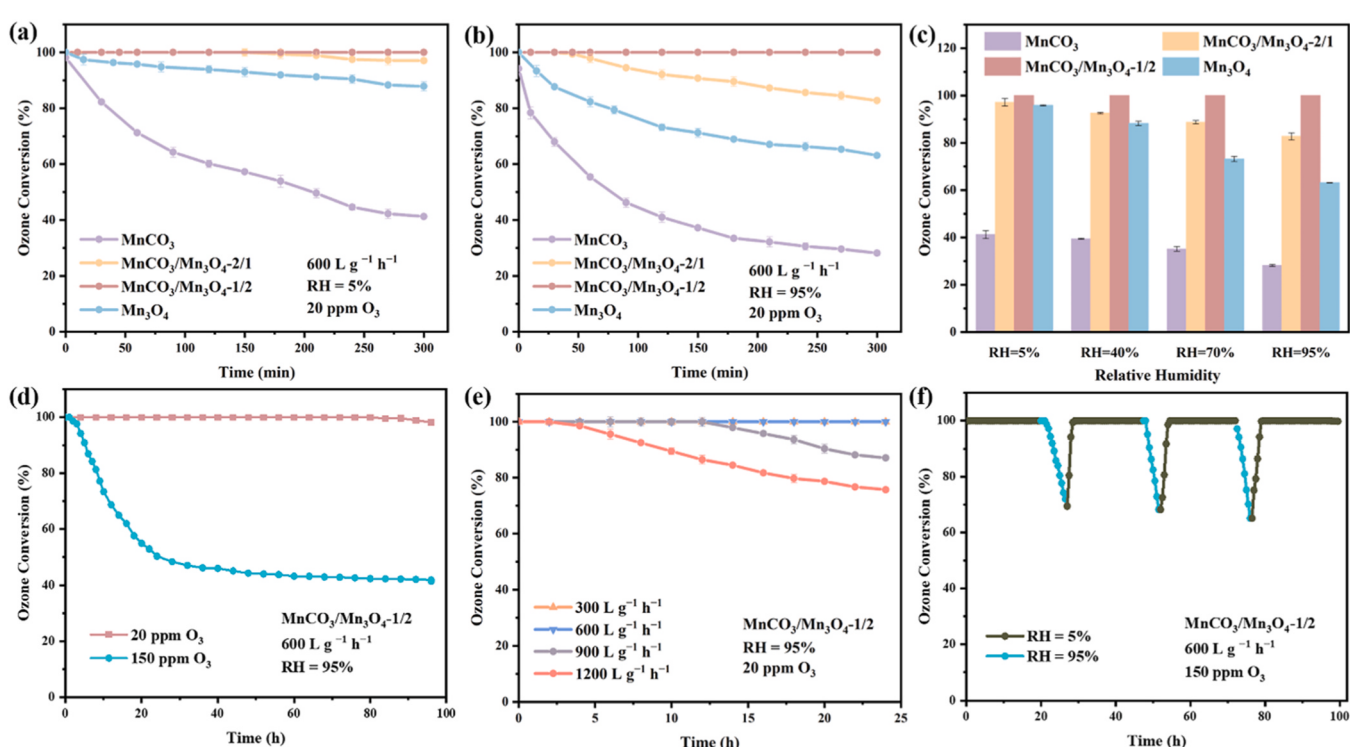
Fig. 3. (a-c) Performance of $MnCO_3$, $MnCO_3/Mn_3O_4$-2/1, $MnCO_3/Mn_3O_4$-1/2 and Mn_3O_4 catalysts for ozone decomposition at different humidity (WHSV: 600 L $g^{-1}h^{-1}$, O_3: 20 ppm); (d) performance of $MnCO_3/Mn_3O_4$-1/2 for ozone decomposition with different ozone concentration (WHSV: 600 L $g^{-1}h^{-1}$, RH = 95 %); (e) performance of $MnCO_3/Mn_3O_4$-1/2 for ozone decomposition at different WHSVs (RH = 95 %, O_3: 20 ppm); (f) performance of $MnCO_3/Mn_3O_4$-1/2 for ozone decomposition during the alternation of dry (RH =5 %) and humid (RH =95 %) air. Experimental conditions: 30 mg of catalysts, flow rate = 300 mL min^{-1}, 25 °C.

decomposition of lower ozone concentrations. Furthermore, the performance of $MnCO_3/Mn_3O_4$-1/2 was further tested in a broader range of space velocities under 95 % RH (as shown in Fig. 3e). When the space velocity was increased to 1200 L g^{-1} h^{-1}, a notable reduction in the ozone conversion of $MnCO_3/Mn_3O_4$-1/2 took place after 4 hours and decreased up to 75 % after 24 hours, indicating that the stability of ozone degradation decreased with an increase in space velocity. To better understand the effect of water molecules on the performance of catalysts, a high-concentration ozone degradation test was performed on $MnCO_3/Mn_3O_4$-1/2 with alternating dry and wet conditions (5 % and 95 % RH, respectively) (Fig. 3 f). Initially, the ozone conversion rate was maintained at 100 % at 5 % RH, while as a consequence of the change to 95% RH, it gradually decreased to 80 % after 5 h. When the RH drops from 95 % to 5 %, the ozone-conversion efficiency can promptly recover to 100 %, which suggests that the $MnCO_3/Mn_3O_4$-1/2 has weak H_2O

adsorption. In addition, low-concentration ozone degradation tests were performed on $MnCO_3$ and Mn_3O_4, as a comparison, as shown in Fig. S6. The performance of $MnCO_3$ and Mn_3O_4, especially Mn_3O_4, could not be fully recovered to the performance at a continuous RH of 5 % after the RH was reduced from 95 % to 5 %, indicating that the distinctive heterogeneous structures enabled significant improvement in the water resistance of the ozone decomposition catalyst.

3.3. Ozone decomposition mechanism

Oyama et al. proposed a three-step sequence for the decomposition of ozone on transition metal oxide, including the dissociation of adsorbed ozone into oxygen atoms and molecules (Step 1), the reaction between oxygen atoms and gaseous ozone molecules resulting in adsorbed intermediate oxygen species (O_2^{2-}) and gas-phase oxygen (Step 2), and
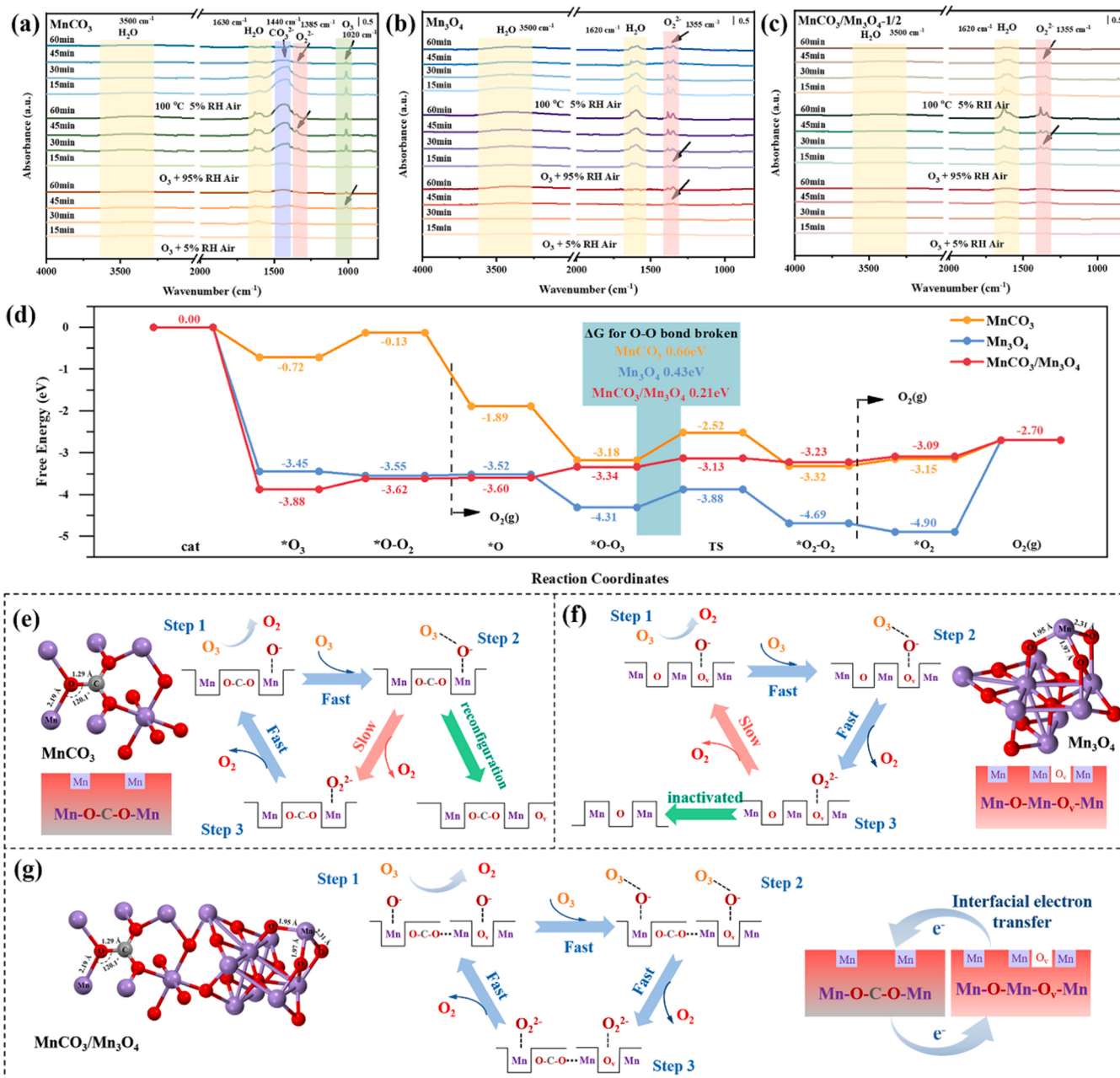
Fig. 4. In-situ DRIFT spectra of (a) $MnCO_3$, (b) Mn_3O_4, and (c) $MnCO_3/Mn_3O_4$-1/2 under ozone-dry air, ozone-wet air, and dry air conditions. (d) Free energy diagrams of O_3 decomposition over $MnCO_3$, Mn_3O_4, and $MnCO_3/Mn_3O_4$ under dry conditions. Schematic representations and ozone decomposition illustration of (e) $MnCO_3$, (f) Mn_3O_4, and (g) $MnCO_3/Mn_3O_4$.

the subsequent desorption of O_2^{2-} into molecular oxygen (Step 3) [12, 15]. The symbol * represents the reaction site on the catalyst surface, and the reaction process can be clearly illustrated by the following equation.

$$O_3 + ^* \rightarrow O_2 + O^* \tag{1}$$

$$O_3 + O^* \rightarrow O_2 + O_2^* \tag{2}$$

$$O_2^* \rightarrow O_2 + ^* \tag{3}$$
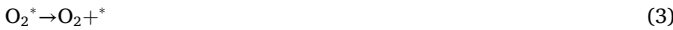
The initial step is speedy, whereas the subsequent two steps occur relatively slowly, determining the rate and amount of accumulation of O_2^* on the catalyst surface. The third step is usually the slowest and the rate-determining step in the ozone decomposition of manganese oxide [20,33].

In-situ diffuse reflectance Fourier transform infrared (DRIFT) spectroscopy can be used to study adsorbed intermediates during ozone decomposition. Ozone decomposition was dynamically investigated on several catalysts by undertaking in-situ DRIFT measurements under ozone-dry air, ozone-wet air, and final dry air conditions, as shown in Fig. 4a-c. In the in-situ DRIFT under ozone-dry air conditions, a signal of surface-adsorbed ozone molecules was detected near 1020 cm^{-1} on the surface of MnCO$_3$ after 45 min, suggesting that ozone molecules can easily accumulate on the surface of MnCO$_3$ (Fig. 4a). Subsequently, after 60 min, a weak signal peak was detected at 1440 cm^{-1}, which was attributed to the surface adsorption of carbonate adsorption peaks [27]. It was hypothesized that the MnCO$_3$ surface was partially oxidized by oxygen to form MnO$_x$, and CO$_2$ was generated to be adsorbed as carbonate on the catalyst surface. Combined with the decomposition stability test of MnCO$_3$ over a long period in dry ozone gas (Fig. S7), the performance of MnCO$_3$ increased after a sharp decrease. Furthermore, combining HRTEM of fresh MnCO$_3$, O$_3$-induced MnCO$_3$ and used MnCO$_3$ after 80 h of reaction (Fig. S8), it was found that the O$_3$-induced MnCO$_3$ showed obvious irregular protrusions at the edges, and the edges of the catalyst appeared to be encapsulated after 80 h of reaction, whereas the fresh catalyst had smooth boundaries and well-defined lattice stripes. It is reasonable to assume that the manganese oxide formed during ozone decomposition is the key active component of MnCO$_3$ during the long ozone decomposition process. However, due to the short duration of the in-situ DRIFT test, it was not sufficient to oxidize most of the MnCO$_3$ surface, and it is believed that it still shows the adsorption state of the reaction intermediates on the MnCO$_3$ surface. In the in-situ DRIFT under ozone-wet air conditions, the peak of surface adsorbed carbonate at 1440 cm^{-1} of MnCO$_3$ was significantly enhanced after the introduction of water vapor for 30 min. In addition, after cutting off ozone and water vapor and increasing the temperature to 100 °C, the adsorption peaks of O_2^{2-} species on the surface of MnCO$_3$ at 1355 cm^{-1} gradually weakened and disappeared after 45 min. The fact that the O_2^{2-} species, an intermediate product of ozone decomposition, can be desorbed indicates that the adsorption is relatively weak [20,36, 42]. Thus, due to the rapid accumulation of ozone molecules and the rapid desorption of O_2^{2-}, it is suggested that the rate-determining step of ozone decomposition on the MnCO$_3$ surface is not the desorption of O_2^{2-} into molecular oxygen.

For Mn$_3$O$_4$ (Fig. 4b), in the in-situ DRIFT under ozone-dry air conditions, a new signal was generated at 1355 cm^{-1} after 45 min, attributed to the adsorption peak of the O_2^{2-} oxygen species [43]. In particular, the adsorption peak attributed to H$_2$O at 1620 cm^{-1} was significantly enhanced after introducing water vapor for 15 min, whereas the adsorption peak of O_2^{2-} oxygen species was significantly weakened compared to its adsorption peak under ozone-dry air conditions. It is assumed that the rate of O_2^{2-} accumulation was slowed down due to the competitive adsorption of H$_2$O. In addition, O_2^{2-} continued to be adsorbed even after cutting off ozone and water vapor and increasing the temperature to 100 °C for 60 min, indicating that O_2^{2-} was strongly adsorbed on the Mn$_3$O$_4$ surface [44]. Therefore, the desorption of O_2^{2-} is

considered to be a decisive step in the ozone decomposition process on the Mn$_3$O$_4$ surface.

For MnCO$_3$/Mn$_3$O$_4$, as shown in Fig. 4c, no new signals were detected in the dry ozone stream, suggesting that there was no O_2^{2-} accumulation on the surface of MnCO$_3$/Mn$_3$O$_4$ comparable to that on the surface of Mn$_3$O$_4$. After the introduction of water vapor, weak O_2^{2-} peaks and water-related peaks appeared at 1355 cm^{-1} and 1620 cm^{-1}, indicating a gradual accumulation of O_2^{2-} as the reaction proceeded [45]. Furthermore, after cutting off the ozone and water vapor and increasing the temperature to 100 °C, the O_2^{2-} peaks rapidly weakened and disappeared, suggesting that O_2^{2-} adsorbs weakly on the MnCO$_3$/Mn$_3$O$_4$ surface and is more readily desorbed. Although some of the Mn-O$_v$ sites may be occupied by water molecules in the humid ozone stream, resulting in the reduction of ozone-active sites, the efficient electron migration between MnCO$_3$ and Mn$_3$O$_4$ ensures that the ozone decomposition efficiency remains at a high level. Combined with the ozone decomposition performance of MnCO$_3$/Mn$_3$O$_4$ under different humidity conditions, it can be determined that the synergistic effect of MnCO$_3$ and Mn$_3$O$_4$ leads to the rapid completion of steps 2 and 3.

For the MnCO$_3$, Mn$_3$O$_4$ and MnCO$_3$/Mn$_3$O$_4$ catalysts, we calculated the reaction energies for each of the basic reactions in the ozone decomposition process separately, as shown in Fig. 4d. It can be seen that the generation of O_2^{2-} on the surface of MnCO$_3$ is the limiting step in the catalytic cycle (0.66 eV), this is limited by the slow O-O bond broken kinetics of MnCO$_3$. Whereas the desorption of O_2^{2-} is the limiting step in the last step for both Mn$_3$O$_4$ and MnCO$_3$/Mn$_3$O$_4$. In addition, the energy barrier of MnCO$_3$/Mn$_3$O$_4$ is lower (0.39 eV) at the last step compared to Mn$_3$O$_4$ implies that the desorption of O_2^{2-} by MnCO$_3$/Mn$_3$O$_4$ is easier.

Combining the above results, the ozone decomposition proceeds of MnCO$_3$, Mn$_3$O$_4$ and MnCO$_3$/Mn$_3$O$_4$ are illustrated in Fig. 4e-g. For MnCO$_3$, the ozone molecules are initially adsorbed on the Mn-O-C site and adsorbed in O$^-$ form after the desorption of an oxygen molecule. This process partially oxidizes the MnCO$_3$ surface, resulting in the formation of discontinuous MnO$_x$. As the reaction proceeds, the Mn-O$_v$ of the MnO$_x$ continues to participate as the active site. The O$^-$ adsorbed on the active site continues to react with O$_3$ to form O_2^{2-}, and the reaction progresses slowly due to the small number of active sites. As for Mn$_3$O$_4$, the number of oxygen ligands around the manganese site decreases from six to five due to the presence of surface oxygen vacancies, which are considered to be active sites for ozone decomposition. Ozone molecules initially attach to the active site of Mn-O$_v$ and are adsorbed on the site in O$^-$ form after successful desorption of one oxygen molecule. Then the O$^-$ adsorbed on the active site will continue to react with O$_3$ to form O_2^{2-}. However, the desorption of O_2^{2-} is more challenging, leading to its accumulation on the surface of Mn$_3$O$_4$, which consumes oxygen vacancies and accelerates catalyst deactivation. In addition, the rapid electron migration on the surface of the MnCO$_3$/Mn$_3$O$_4$ catalyst and at the interface of the two phases accelerated the decomposition of ozone and prevented catalyst deactivation. In conclusion, the unique heterogeneous structure of MnCO$_3$/Mn$_3$O$_4$ provides high and stable ozone decomposition performance.

3.4. Ozone atmosphere-induced reconfiguration of catalysts

Combined with the In-situ DRIFT results of MnCO$_3$ catalyst under the ozone atmosphere, the phenomenon of surface adsorption of carbonate species indicates that the structure of the heterogeneous catalysts would be reconstructed during the catalytic reaction. To clarify the catalyst reconstruction process, the structure of the MnCO$_3$/Mn$_3$O$_4$-1/2 catalyst after 0.5 h ozone atmosphere treatment was characterized. As shown in Fig. 5a-c, HRTEM results show that discontinuous irregular protrusions are observed at the edge of MnCO$_3$ in the heterostructure catalyst after being treated in an ozone atmosphere for 0.5 hours. The XPS C 1 s spectrum of MnCO$_3$/Mn$_3$O$_4$-1/2 before and after ozone treatment shows that the peak value of CO$_3^{2-}$ is slightly reduced after ozone treatment, further proving that the surface of MnCO$_3$ is partially oxidized to form
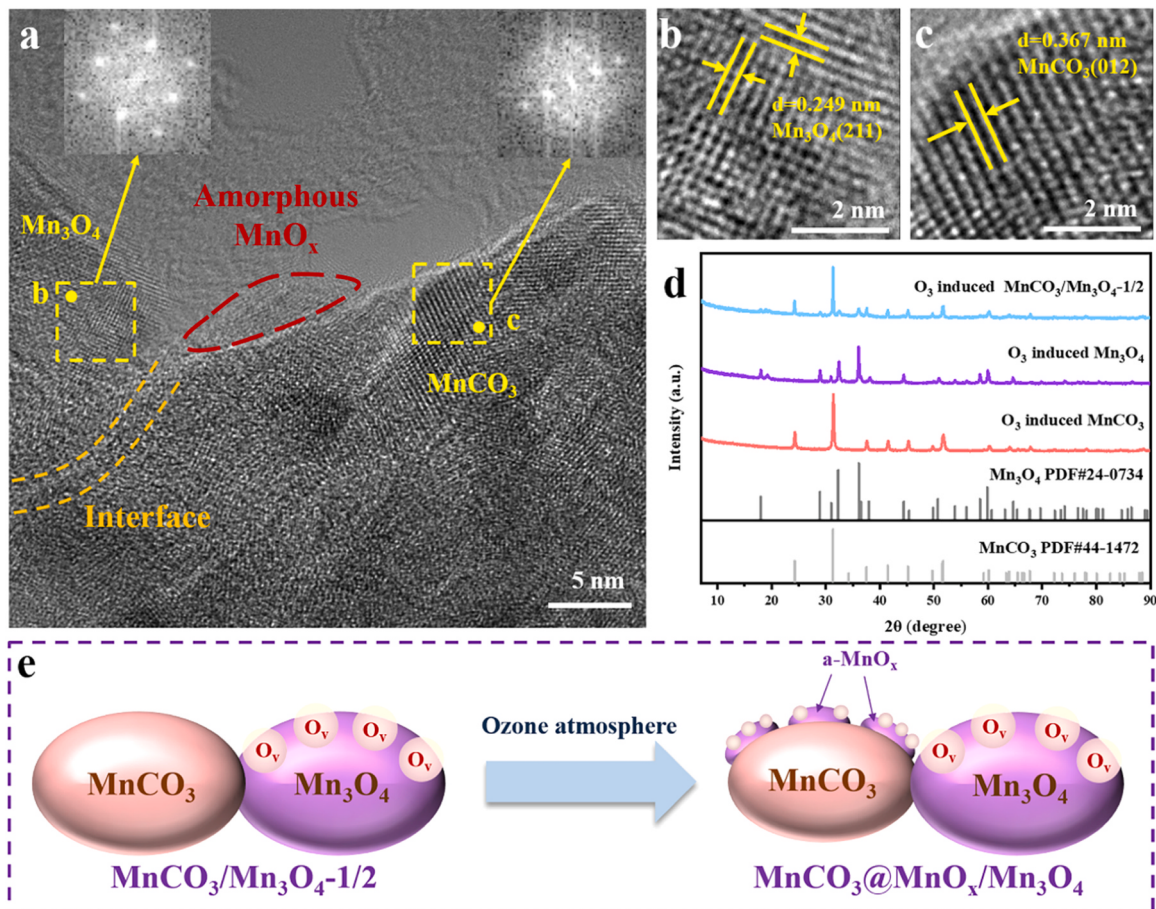
Fig. 5. (a-c) HRTEM images for O_3-induced $MnCO_3/Mn_3O_4$-1/2 catalyst. (d) XRD patterns for O_3-induced $MnCO_3$, $MnCO_3/Mn_3O_4$-1/2 and Mn_3O_4 catalysts. (e) Schematic representations of $MnCO_3/Mn_3O_4$-1/2 reconfiguration induced by ozone atmosphere.

MnO_x (Fig. S9). In addition, the XRD spectrum of the catalyst after ozone atmosphere treatment showed that no new diffraction peaks appeared, indicating that MnO_x was analyzed as an amorphous form on the surface of $MnCO_3$, as shown in Fig. 5d. The above results display that $MnCO_3/Mn_3O_4$ undergoes reconstruction under ozone atmosphere, inducing discontinuous amorphous MnO_x on the $MnCO_3$ surface and forming the $MnCO_3@MnO_x/Mn_3O_4$ structure (Fig. 5e).

3.5. Stability mechanism of $MnCO_3/Mn_3O_4$-1/2 composite catalyst in ozone decomposition reaction

To further clarify the role of heterogeneous structure of $MnCO_3/Mn_3O_4$ catalyst in the ozone decomposition process, the structural changes of the used $MnCO_3/Mn_3O_4$-1/2 catalyst were evaluated. The XRD spectrum shown in Fig. S10 indicates that the diffraction peak signals of $MnCO_3$ and Mn_3O_4 are still discernible after use [46,47]. In addition, weak new diffraction peaks at 23.1° and 55.1° attributed to Mn_2O_3 (PDF card no. 41–1442) appeared in the used catalysts, indicating that partially adsorbed reaction intermediates on the surface of the $MnCO_3/Mn_3O_4$ catalysts were converted to lattice oxygen after a long period of ozone decomposition reaction, which led to the formation of a small amount of Mn_2O_3. As shown in Fig. S11 and Table S2, the Mn 2p signals show a slight decrease in the Mn^{2+}/Mn^{3+} ratio of the used $MnCO_3/Mn_3O_4$-1/2 catalysts compared to the fresh catalysts, and the binding energy is shifted by 0.5 eV in the high-energy direction, indicating that the surface manganese is partially oxidized. Furthermore, SEM images (Fig. S12) showed that the overall morphology and structure of the catalyst did not show any significant changes after the reaction. The HRTEM images showed a slight accumulation of amorphous

MnO_x structures at the edges of the catalyst particles compared with the ozone atmosphere reconstructed catalyst, but no continuous coating layer was formed (Fig. S13). The results indicate that the morphological structure of $MnCO_3/Mn_3O_4$-1/2 catalyst remained stable throughout the ozone decomposition reaction, without significant changes.

Combined with the performance differences among the series of catalysts and the widely reported promotion effect of oxygen vacancies to ozone decomposition, the contribution of heterogeneous interfacial structure to the reaction process was further explored by EPR, CV curves and EIS. In the EPR spectra (Fig. S14), the fresh and used catalysts showed a distinct peak at g = 2.003, with the fresh catalyst having a slightly larger peak intensity and a relatively higher number of surface oxygen vacancies [48,49]. In addition, as shown in Fig. S15, the oxidation peak areas in the CV curves as well as the radii of the Nyquist circles in the EIS plots showed a similar trend between the fresh and used catalysts, suggesting that the concentration of the oxygen vacancies and the electron mobility rate changed less after the catalysts were used [36, 50]. In conclusion, the above results showed that the overall oxygen vacancy content of the $MnCO_3/Mn_3O_4$-1/2 catalysts remained relatively stable and electron mobility remained almost unchanged after the ozone decomposition reaction.

Based on these results, the structural evolution of the $MnCO_3/Mn_3O_4$-1/2 catalyst in the ozone decomposition reaction is summarized (as shown in Scheme S1). Following the reaction initiation, $MnCO_3$ contributes electrons and forms MnO_x layer containing a large number of oxygen vacancies on the surface, and the oxygen vacancies on the surface of Mn_3O_4 also donate electrons. These electrons are utilized in the first two stages of the ozone decomposition process as shown in Eqs. (S1)–(5). As the desorption of the intermediate peroxide (O_2^-) is the rate-

determining step of Mn_3O_4, the formed O_2^{2-} occupies some of the active sites on the Mn_3O_4 surface. Simultaneously, electron transfer takes place at the MnO_x/Mn_3O_4 interface, as shown in Eqs. (S6)–(8), leading to the detachment of O_2^{2-} from the electron-deficient Mn_3O_4 surface and the release of electrons. As the reaction proceeds, the MnO_x deposited on the surface of $MnCO_3$ contributes electrons and gradually participates in Eq. (S4), accelerating the electron transfer on the catalyst surface. Combined with changes in the catalyst structure, it is assumed that $MnCO_3$ formed discontinuous MnO_x as a surface layer during the reaction, providing a charge potential energy difference and accelerating the overall electron migration of the catalyst. In conclusion, the electronic state of the active site during the reaction process was modulated by the heterogeneous structure of $MnCO_3/Mn_3O_4$, which exerted an interfacial effect to accelerate the rate-determining step of $MnCO_3$ and Mn_3O_4, thus promoting the high-performance decomposition of ozone.

4. Conclusion

In this work, we successfully synthesized a series of single-phase catalysts and $MnCO_3/Mn_3O_4$ composite catalysts by co-precipitation, and optimized the heterogeneous structure by adjusting the ratio of OH^-/CO_3^{2-} in the precursor solution. The heterogeneous structures of $MnCO_3/Mn_3O_4$ could regulate the electronic state of the active site, increase the abundance of oxygen vacancies, and enhance the rate of electron mobility. The ozone conversion of $MnCO_3/Mn_3O_4$-1/2 remained above 95% after 100 h of reaction under the conditions of initial ozone concentration of 20 ppm, relative humidity of 95%, and space velocity of 600 L g $^{-1}$ h^{-1}, which was much better than that of $MnCO_3$ and Mn_3O_4 catalysts. The in-situ DRIFT results show that the rate-determining steps for the ozone decomposition reactions of $MnCO_3$ and Mn_3O_4 are the reaction of atomic oxygen with ozone to form O_2^{2-} and the desorption of intermediate peroxides (O_2^{2-}), respectively. $MnCO_3/Mn_3O_4$ heterogeneous catalyst undergoes reconfiguration under ozone atmosphere, inducing discontinuous MnO_x coatings on the $MnCO_3$ surface, which form a potential difference with Mn_3O_4. The synergistic effect of $MnCO_3$ and Mn_3O_4 accelerates the two rate-determining steps, resulting in excellent ozone decomposition performance throughout the humidity range, which provides a deeper understanding of the ozone decomposition process and contributes to the practical application of manganese-based catalysts.

CRediT authorship contribution statement

Lecheng Lei: Funding acquisition. **Xiangyu Tian:** Methodology, Investigation. **Hao Cheng:** Methodology. **Ning Cao:** Validation, Software, Methodology, Conceptualization. **Yani Zhang:** Writing – original draft, Visualization, Validation, Supervision, Methodology, Data curation, Conceptualization. **Xingwang Zhang:** Writing – review & editing, Funding acquisition, Conceptualization. **Pengfei Xie:** Writing – review & editing, Project administration, Conceptualization. **Jiahong Liao:** Software, Resources, Project administration, Methodology. **Yunlong Fang:** Funding acquisition, Conceptualization. **Lixia Qiu:** Funding acquisition. **Xinben Zhao:** Investigation, Conceptualization. **Xinuo Cai:** Investigation, Formal analysis, Data curation.

Declaration of Competing Interest

We declare that we have no financial or personal relationships with other people or organizations that can inappropriately influence our work. There is no professional or other personal interest of any nature or kind in any product, service and/or company that could be construed as influencing the position presented in, or the review of, the manuscript entitled.

Data Availability

Data will be made available on request.

Appendix A. Supporting information

Supplementary data associated with this article can be found in the online version at doi:10.1016/j.apcatb.2024.124171.

References

[1] P.D. Ivatt, M.J. Evans, A.C. Lewis, Suppression of surface ozone by an aerosol-inhibited photochemical ozone regime, Nat. Geosci. 15 (2022) 536–540, https://doi.org/10.1038/s41561-022-00972-9.

[2] T. Tao, Y. Shi, K.M. Gilbert, X. Liu, Spatiotemporal variations of air pollutants based on ground observation and emission sources over 19 Chinese urban agglomerations during 2015–2019, Sci. Rep. 12 (2022) 4293, https://doi.org/10.1038/s41598-022-08377-9.

[3] K. Li, D.J. Jacob, H. Liao, Y. Qiu, L. Shen, S. Zhai, K.H. Bates, M.P. Sulprizio, S. Song, X. Lu, Q. Zhang, B. Zheng, Y. Zhang, J. Zhang, H.C. Lee, S.K. Kuk, Ozone pollution in the North China Plain spreading into the late-winter haze season, Proc. Natl. Acad. Sci. 118 (2021) e2015797118, https://doi.org/10.1073/pnas.2015797118.

[4] J.L. Crooks, R. Licker, A.L. Hollis, B. Ekwurzel, The ozone climate penalty, NAAQS attainment, and health equity along the Colorado Front Range, J. Expo. Sci. Environ. Epidemiol. 32 (2022) 545–553, https://doi.org/10.1038/s41370-021-00375-9.

[5] C. Cai, J. Avise, A. Kaduwela, J. DaMassa, C. Warneke, J.B. Gilman, W. Kuster, J. de Gouw, R. Volkamer, P. Stevens, B. Lefer, J.S. Holloway, I.B. Pollack, T. Ryerson, E. Atlas, D. Blake, B. Rappenglueck, S.S. Brown, W.P. Dube, Simulating the weekly cycle of NO_x-VOC-HO_x-O_3 photochemical system in the south coast of California during CalNex-2010 campaign, J. Geophys. Res. Atmos. 124 (2019) 3532–3555, https://doi.org/10.1029/2018JD029859.

[6] S.A. Meo, F.J. Almutairi, A.A. Abukhalaf, O.M. Alessa, T. Al-Khlaiwi, A.S. Meo, Sandstorm and its effect on particulate matter PM 2.5, carbon monoxide, nitrogen dioxide, ozone pollutants and SARS-CoV-2 cases and deaths, Sci. Total Environ. 795 (2021) 148764, https://doi.org/10.1016/j.scitotenv.2021.148764.

[7] W.J.M. Seviour, Good ozone, bad ozone and the Southern Ocean, Nat. Clim. Change 12 (2022) 316–317, https://doi.org/10.1038/s41558-022-01322-8.

[8] A. Goshua, C.A. Akdis, K.C. Nadeau, World health organization global air quality guideline recommendations: executive summary, Allergy 77 (2022) 1955–1960, https://doi.org/10.1111/all.15224.

[9] J. Ma, C. Wang, H. He, Transition metal doped cryptomelane-type manganese oxide catalysts for ozone decomposition, Appl. Catal. B Environ. 201 (2017) 503–510, https://doi.org/10.1016/j.apcatb.2016.08.050.

[10] X. Wan, L. Wang, S. Zhang, S. Shi, J. Niu, G. Wang, W. Li, D. Chen, H. Zhang, X. Zhou, W. Wang, Ozone decomposition below room temperature using Mn-based mullite YMn_2O_5, Environ. Sci. Technol. 56 (2022) 8746–8755, https://doi.org/10.1021/acs.est.1c08922.

[11] Z. Wang, Y. Chen, X. Li, G. He, J. Ma, H. He, Layered double hydroxide catalysts for ozone decomposition: the synergic role of M^{2+} and M^{3+}, Environ. Sci. Technol. 56 (2022) 1386–1394, https://doi.org/10.1021/acs.est.1c07829.

[12] B. Dhandapani, S.T. Oyama, Gas phase ozone decomposition catalysts, Appl. Catal. B Environ. 11 (1997) 129–166, https://doi.org/10.1016/S0926-3373(96)00044-6.

[13] M. Namdari, C.-S. Lee, F. Haghighat, Active ozone removal technologies for a safe indoor environment: a comprehensive review, Build. Environ. 187 (2021) 107370, https://doi.org/10.1016/j.buildenv.2020.107370.

[14] H. Li, P. Zhang, J. Jia, X. Wang, S. Rong, A cobalt-vacant Co_3O_4 as a stable catalyst for room-temperature decomposition of ozone in humid air, Appl. Catal. B Environ. 340 (2024) 123222, https://doi.org/10.1016/j.apcatb.2023.123222.

[15] W. Li, S.T. Oyama, Mechanism of ozone decomposition on a manganese oxide catalyst. 2. steady-state and transient kinetic studies, J. Am. Chem. Soc. 120 (1998) 9047–9052, https://doi.org/10.1021/ja9814422.

[16] G. Zhu, J. Zhu, W. Jiang, Z. Zhang, J. Wang, Y. Zhu, Q. Zhang, Surface oxygen vacancy induced α-MnO_2 nanofiber for highly efficient ozone elimination, Appl. Catal. B Environ. 209 (2017) 729–737, https://doi.org/10.1016/j.apcatb.2017.02.068.

[17] X. Li, J. Ma, L. Yang, G. He, C. Zhang, R. Zhang, H. He, Oxygen vacancies induced by transition metal doping in γ-MnO$_2$ for highly efficient ozone decomposition, Environ. Sci. Technol. 52 (2018) 12685–12696, https://doi.org/10.1021/acs. est.8b04294.

[18] G. Zhu, J. Zhu, W. Li, W. Yao, R. Zong, Y. Zhu, Q. Zhang, Tuning the K$^+$ concentration in the tunnels of α-MnO$_2$ to increase the content of oxygen vacancy for ozone elimination, Environ. Sci. Technol. 52 (2018) 8684–8692, https://doi. org/10.1021/acs.est.8b01594.

[19] J.-M. Tatibouët, S. Valange, H. Touati, Near-ambient temperature ozone decomposition kinetics on manganese oxide-based catalysts, Appl. Catal. A Gen. 569 (2019) 126–133, https://doi.org/10.1016/j.apcata.2018.10.026.

[20] Z. Wu, P. Zhang, S. Rong, J. Jia, Creating water-resistant oxygen vacancies in δ-MnO$_2$ by chlorine introduction for catalytic ozone decomposition at ambient temperature, Appl. Catal. B Environ. 335 (2023) 122900, https://doi.org/ 10.1016/j.apcatb.2023.122900.

[21] J. Jia, P. Zhang, L. Chen, Catalytic decomposition of gaseous ozone over manganese dioxides with different crystal structures, Appl. Catal. B Environ. 189 (2016) 210–218, https://doi.org/10.1016/j.apcatb.2016.02.055.

[22] J. Ma, R. Cao, Y. Dang, J. Wang, A recent progress of room–temperature airborne ozone decomposition catalysts, Chin. Chem. Lett. 32 (2021) 2985–2993, https:// doi.org/10.1016/j.cclet.2021.03.031.

[23] R. Zhang, S. Li, A. Zhang, Y. Zhang, J. Guo, F. Dong, Y. Zhou, Mn-N/C interfacial bridge accelerating electrons transfer of MnCO$_3$/α-Ni(OH)$_2$ to promote surface adsorbates activation for favorable photocatalytic NO oxidation, J. Environ. Chem. Eng. 11 (2023) 110244, https://doi.org/10.1016/j.jece.2023.110244.

[24] H. Shen, M. Luo, J. Wang, M. Li, Z. He, H. Zhong, W. Sun, M. Ye, Y. Tang, Self-formed MnCO$_3$/FeS$_2$@SiO$_2$ in modified electrolytic manganese residues as an enhanced peroxymonosulfate activator for ammonium dibutyl dithio-phosphate removal, Chem. Eng. J. 472 (2023) 144915, https://doi.org/10.1016/j. cej.2023.144915.

[25] S. Wu, C. Liu, D.A. Dinh, K.S. Hui, K.N. Hui, J.M. Yun, K.H. Kim, Three-dimensional self-standing and conductive MnCO$_3$@Graphene/CNT networks for flexible asymmetric supercapacitors, ACS Sustain. Chem. Eng. 7 (2019) 9763–9770, https://doi.org/10.1021/acssuschemeng.8b05935.

[26] L. Lamaita, M.A. Peluso, J.E. Sambeth, H.J. Thomas, Synthesis and characterization of manganese oxides employed in VOCs abatement, Appl. Catal. B Environ. 61 (2005) 114–119, https://doi.org/10.1016/j.apcatb.2005.03.014.

[27] J. Jia, P. Zhang, Catalytic decomposition of airborne ozone by MnCO$_3$ and its mechanism, Ozone Sci. Eng. 40 (2018) 21–28, https://doi.org/10.1080/ 01919512.2017.1328272.

[28] Y. Liu, P. Zhang, J. Zhan, L. Liu, Heat treatment of MnCO$_3$: an easy way to obtain efficient and stable MnO$_2$ for humid O$_3$ decomposition, Appl. Surf. Sci. 463 (2019) 374–385, https://doi.org/10.1016/j.apsusc.2018.08.226.

[29] G. Wang, B. Huang, Z. Lou, Z. Wang, X. Qin, X. Zhang, Y. Dai, Valence state heterojunction Mn$_3$O$_4$/MnCO$_3$: photo and thermal synergistic catalyst, Appl. Catal. B Environ. 180 (2016) 6–12, https://doi.org/10.1016/j.apcatb.2015.06.010.

[30] R. Zhang, D. Wang, L.-C. Qin, G. Wen, H. Pan, Y. Zhang, N. Tian, Y. Zhou, X. Huang, MnCO$_3$/Mn$_3$O$_4$/reduced graphene oxide ternary anode materials for lithium-ion batteries: facile green synthesis and enhanced electrochemical performance, J. Mater. Chem. A. 5 (2017) 17001–17011, https://doi.org/10.1039/ C7TA02874A.

[31] H. Wang, P. Rassu, X. Wang, H. Li, X. Wang, X. Wang, X. Feng, A. Yin, P. Li, X. Jin, S.-L. Chen, X. Ma, B. Wang, An iron-containing metal–organic framework as a highly efficient catalyst for ozone decomposition, Angew. Chem. Int. Ed. 57 (2018) 16416–16420, https://doi.org/10.1002/anie.201810268.

[32] M. Qi, L. Lin, L. Wang, Z. Bai, Y. Yu, J. Gu, Y. Liu, Spindle MnCO$_3$ tightly encapsulated by MXene nanoflakes with strengthened interface effect for lithium-ion battery, Surf. Coat. Tech. 417 (2021) 127192, https://doi.org/10.1016/j. surfcoat.2021.127192.

[33] L. Zhang, J. Yang, A. Wang, S. Chai, J. Guan, L. Nie, G. Fan, N. Han, Y. Chen, High performance ozone decomposition spinel (Mn,Co)$_3$O$_4$ catalyst accelerating the rate-determining step, Appl. Catal. B Environ. 303 (2022) 120927, https://doi.org/ 10.1016/j.apcatb.2021.120927.

[34] S. Wang, Y. Zhu, Y. Zhang, B. Wang, H. Yan, W. Liu, Y. Lin, Manganese-based layered double hydroxide nanoparticles as highly efficient ozone decomposition catalysts with tunable valence state, Nanoscale 12 (2020) 12817–12823, https:// doi.org/10.1039/D0NR02796K.

[35] Y. Zhang, X. Zhang, P. Yang, M. Gao, J. Feng, D. Li, In situ topologically induced PtZn alloy @ ZnTiO$_x$ and the synergistic effect on glycerol oxidation, Appl. Catal. B Environ. 298 (2021) 120634, https://doi.org/10.1016/j.apcatb.2021.120634.

[36] W. Dai, B. Zhang, J. Ji, B. Liu, R. Xie, Y. Gan, X. Xie, J. Zhang, P. Huang, H. Huang, Exceptional ozone decomposition over δ-MnO$_2$/AC under an entire humidity environment, Environ. Sci. Technol. (2023), https://doi.org/10.1021/acs. est.3c00717.

[37] G. Zhu, W. Zhu, Y. Lou, J. Ma, W. Yao, R. Zong, Y. Zhu, Encapsulate α-MnO$_2$ nanofiber within graphene layer to tune surface electronic structure for efficient ozone decomposition, Nat. Commun. 12 (2021) 4152, https://doi.org/10.1038/ s41467-021-24424-x.

[38] B. Liu, Z. Yi, Y. Yang, Y. Li, J. Yang, M. Zhu, Unlocking efficient and robust ozone decomposition with CNT-confined manganese oxide via synergistic electronic modulation, Appl. Catal. B Environ. 334 (2023) 122788, https://doi.org/10.1016/ j.apcatb.2023.122788.

[39] X. Tian, W. Han, Z. Zeng, Y. He, L. Lei, X. Xu, X. Xu, Y. Xu, P. Li, X. Zhang, Oleyl phosphate-modified crystalline-amorphous TiO$_2$/Ce$_2$O$_3$ heterojunction nanoparticles with significantly reduced photocatalytic activity as stable UV-shielding fillers, Chem. Eng. J. 477 (2023) 146962, https://doi.org/10.1016/j. cej.2023.146962.

[40] Y.-H. Zhang, M.-X. Peng, L.-J. Yue, J.-L. Chen, F.-L. Gong, K.-F. Xie, S.-M. Fang, A room-temperature aniline sensor based on Ce doped ZnO porous nanosheets with abundant oxygen vacancies, J. Alloy. Compd. 885 (2021) 160988, https://doi.org/ 10.1016/j.jallcom.2021.160988.

[41] Y. Zhao, C. Chang, F. Teng, Y. Zhao, G. Chen, R. Shi, G.I.N. Waterhouse, W. Huang, T. Zhang, Defect-engineered ultrathin δ-MnO$_2$ nanosheet arrays as bifunctional electrodes for efficient overall water splitting, Adv. Energy Mater. 7 (2017) 1700005, https://doi.org/10.1002/aenm.201700005.

[42] K.B. Nam, D.W. Kwon, S.C. Hong, DRIFT study on promotion effects of tungsten-modified Mn/Ce/Ti catalysts for the SCR reaction at low-temperature, Appl. Catal. A Gen. 542 (2017) 55–62, https://doi.org/10.1016/j.apcata.2017.05.017.

[43] W. Hong, M. Shao, T. Zhu, H. Wang, Y. Sun, F. Shen, X. Li, To promote ozone catalytic decomposition by fabricating manganese vacancies in ε-MnO$_2$ catalyst via selective dissolution of Mn-Li precursors, Appl. Catal. B Environ. 274 (2020) 119088, https://doi.org/10.1016/j.apcatb.2020.119088.

[44] W. Hong, J. Ma, T. Zhu, H. He, H. Wang, Y. Sun, F. Shen, X. Li, To enhance water resistance for catalytic ozone decomposition by fabricating H$_2$O adsorption-site in OMS-2 tunnels, Appl. Catal. B Environ. 297 (2021) 120466, https://doi.org/ 10.1016/j.apcatb.2021.120466.

[45] J. Jia, P. Zhang, L. Chen, Catalytic decomposition of gaseous ozone over manganese dioxides with different crystal structures, Appl. Catal. B Environ. 189 (2016) 210–218, https://doi.org/10.1016/j.apcatb.2016.02.055.

[46] J. Ma, X. Li, C. Zhang, Q. Ma, H. He, Novel CeMn$_a$O$_x$ catalyst for highly efficient catalytic decomposition of ozone, Appl. Catal. B Environ. 264 (2020) 118498, https://doi.org/10.1016/j.apcatb.2019.118498.

[47] X. Wang, Z. Wang, Y. Bai, L. Tan, Y. Xu, X. Hao, J. Wang, A.H. Mahadi, Y. Zhao, L. Zheng, Y.-F. Song, Tuning the selectivity of photoreduction of CO$_2$ to syngas over Pd/layered double hydroxide nanosheets under visible light up to 600 nm, J. Energy Chem. 46 (2020) 1–7, https://doi.org/10.1016/j.jechem.2019.10.004.

[48] Z. Huang, T. Ban, Y. Zhang, L. Wang, S. Guo, C.-R. Chang, G. Jing, Boosting the thermal stability and catalytic performance by confining Ag single atom sites over antimony-doped tin oxide via atom trapping, Appl. Catal. B Environ. 283 (2021) 119625, https://doi.org/10.1016/j.apcatb.2020.119625.

[49] D. Xia, D. Liu, B. Xu, Y. Wang, Y. Liao, Y. Huang, L. Ye, C. He, P.K. Wong, R. Qiu, Single Ag atom engineered 3D-MnO$_2$ porous hollow microspheres for rapid photothermocatalytic inactivation of E. coli under solar light, Appl. Catal. B Environ. 245 (2019) 177–189, https://doi.org/10.1016/j.apcatb.2018.12.056.

[50] Y. Wang, C. Zhang, L. Zhang, J. Zeng, H. He, Anti-sulfur selective catalytic reduction of NO$_x$ on Sb-doped OMS-2, Appl. Catal. A Gen. 641 (2022) 118684, https://doi.org/10.1016/j.apcata.2022.118684.